Dielectronic recombination of lithiumlike beryllium: A theoretical and experimental investigation

T. Mohamed, D. Nikolić,* E. Lindroth, S. Madzunkov, M. Fogle, M. Tokman, and R. Schuch†
Stockholm Center for Physics, Astronomy and Biotechnology (SCFAB), Fysikum, S-106 91 Stockholm, Sweden
(Received 8 February 2002; published 28 August 2002)

Recombination spectra of lithiumlike Be ions, taken at the ion storage ring CRYRING, have been investigated with high-energy resolution. The absolute recombination rate coefficient is measured in the center-of-mass energy range 0–5 eV that covers all $\Delta n=0$ core excitations. The results are compared with *ab initio* calculations and show very good agreement in the resonance energy positions. They also agree in the resonance strengths, except close to the $2s_{1/2}\rightarrow 2p_{1/2,3/2}$ core excitation limit and at the zero center-of-mass energy limit. In the first case the calculated rate coefficient exceeds that of the experiment by up to a factor of 1.7 and in the second it undervalues the experiment by 3.1. Interference effects of direct radiative recombination and recombination via doubly excited states are discussed.

DOI: 10.1103/PhysRevA.66.022719 PACS number(s): 34.80.Lx, 31.25.Jf, 32.80.Dz

I. INTRODUCTION

In the description of ionized matter, electron-ion collisions play an important role. Recombination is a particularly interesting outcome of such a collision, both from an applied point of view and for testing our understanding of basic atomic collision phenomena. Recombination data are directly relevant to plasma modeling in fusion and astrophysical research. Here we present results on the recombination of lithiumlike Be. Two fundamental recombination processes are possible when a single ion collides with a single electron. Radiative recombination (RR) is the time inverse of direct photoionization:

$$\mathrm{Be}^{+}+e^{-}\rightarrow \mathrm{Be}^{*}+\hbar\omega, \tag{1}$$

i.e., nonresonant electron capture directly into a vacant bound state. The cross section for RR is inversely proportional to the relative electron-ion energy. It diverges consequently at zero energy, where the recombination probability approaches unity, and decreases smoothly with increasing energy. Dielectronic recombination (DR) is the time inverse of Auger decay, i.e., resonant radiationless capture of a continuum electron by a Be^{+} ion into an intermediate doubly excited autoionizing state Be**, which, with a small but finite probability, decays by photon emission. If the decay occurs to a bound state, recombination is completed,

$$\mathrm{Be}^{+}+e^{-}\rightarrow \mathrm{Be}^{**}\rightarrow \mathrm{Be}^{*}+\hbar\omega. \tag{2}$$

Besides the above-described recombination scenarios, more than one electron can be involved in the collision and the excess energy can then be carried away by another initially free electron. This process is irrelevant in the present study since only high quantum states can be populated, from where the electron is removed by external fields before detection.

Through measurements of DR resonances, properties of doubly excited states, such as energies, radiative decay rates, and autoionization rates can be studied. Li-like ions have been studied extensively during recent years: C^{3+} [1], N^{4+} [2], F^{6+} [3], Ne^{7+} [4], Si^{11+} [5], Cl^{14+} [6], Ar^{15+} [7], Ni^{25+} [8], Cu^{26+} [9], Kr^{33+} [10], Au^{76+} [11], and U^{89+} [12]. The reason is that Li-like ions are relatively simple and their treatment is within the reach of *ab initio* calculations. Still, they provide enough complexity for studying intriguing many-body effects. With the resolution available in storage rings equipped with electron coolers, they often show well-resolved spectra for low center-of-mass (c.m.) collision energies. These spectra are determined by intershell excitations, i.e., $2s_{1/2}\rightarrow 2p_j$ core excitations and the initially free electron is, generally, captured into a Rydberg state. Since the $2s_{1/2}$-$2p_j$ splitting scales with the nuclear charge (Z), but the binding energy of the captured electron scales as Z^2, it is expected that the principal quantum number for the captured electron decreases when lighter systems are studied. With Be^{+} being the lightest Li-like positive ion, the lowest-energy resonances are consequently of the type $(2p^2)\,{}^1S$ and all the $2\ell 3\ell'$ states form resonances.

When both RR and DR are able to bring the ion from a given initial state into the same final state, they cannot be distinguished and their quantum mechanical amplitudes will interfere. When the amplitudes are of similar magnitude this interference should be observable in recombination spectra, in accordance with observations in photoionization spectra where asymmetric line shapes are well known and was put in a theoretical framework several decades ago by Fano [13]. Interference has been reported in a recombination experiment with trapped uranium ions [14], but there is still no theoretical confirmation of the effect in this system. A clear example of RR-DR interference is therefore still missing. As in Be the lowest-energy resonances are $(2p^2)\,{}^1S$ and $2\ell 3\ell'$ doubly excited states, it is a candidate for detection of asymmetry as will be discussed below. The experiment is described in Sec. II and the theoretical framework in Sec. III A. The results are analyzed and discussed in Secs. IV and V.

II. EXPERIMENT

The experiment was carried out with the ion storage ring CRYRING at the Manne Siegbahn Laboratory [15] in Stock-

*Permanent address: Institute of Physics, University of Novi Sad, 21000 Novi Sad, Yugoslavia.
†Corresponding author. Email address: schuch@physto.se

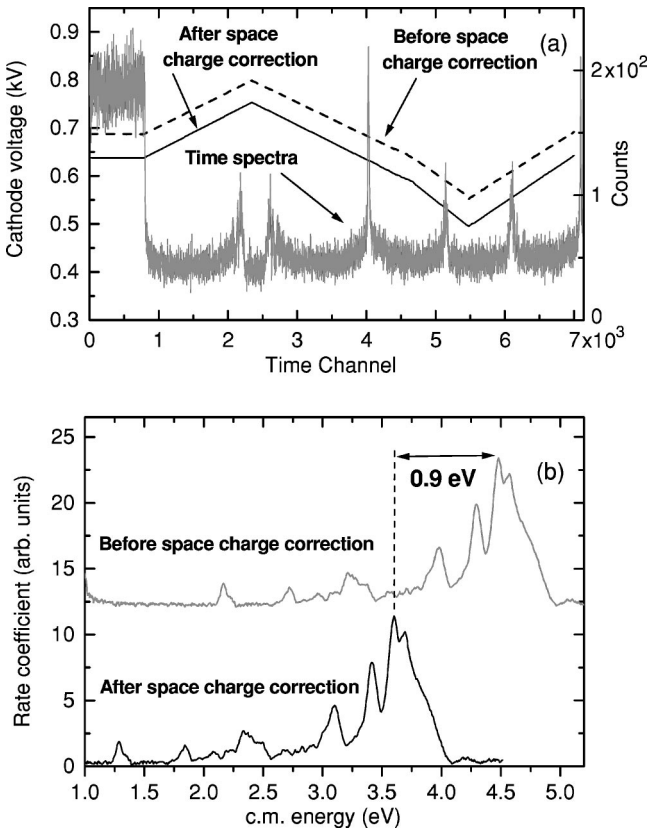

FIG. 1. (a) The gray histogram line represents the number of the recombined ions as a function of the measurement time in each cycle. The dashed line represents the cathode voltage as a function of time before space-charge potential correction. The solid line represents the space-charge-corrected cathode voltage. (b) The gray line shows the spectrum before space-charge potential correction and the black line represents the spectrum after space-charge correction.

holm. The Be^+ beam was produced in a plasmatron ion source and injected into the ring after preacceleration by a radio-frequency quadrupole accelerator to an injection energy of 300 keV/amu. Final acceleration of the ions to an energy of 1.2 MeV/amu was accomplished by a radio-frequency acceleration system while the ions were circulating in the ring. The number of stored ions was estimated to be $\approx 10^7$ from the ion beam current that was measured by an inductive current transformer. Recombined atoms formed in the electron cooler were separated from the circulating beam in the first bending (main dipole) magnet downstream from the cooler, and were detected by a surface barrier detector (SBD) with an efficiency of 100%. The electron cooler was set to provide an electron beam with a transverse temperature ($kT_\perp$) of 1 meV. Once the ion beam is cooled, a scanning of the cathode voltage and data acquisition took place. For each recombination event detected, the cathode voltage and the time related to the scan trigger were recorded. Figure 1(a) shows typical raw data for Be^+ as a histogram representing the number of recombined ions as a function of time. The interaction energy of the electrons with the ions in the cooler was controlled by scanning the cathode voltage of the electron cooler over a certain range that covers all $\Delta n = 0$ core excitations (approximately 5 eV in the c.m. frame). The voltage scan started after cooling the ion beam for 3 and had a zig-zag pattern, i.e., the cathode voltage first went up for 1 s, then down from its maximum, crossing the cooling voltage to reach the minimum after 3 s and back to the cooling voltage again [Fig. 1(a)]. In Fig. 1(a) the dashed line represents the cathode voltage scan before space-charge potential correction that will be discussed in details in Sec. IV. The solid line represents the cathode voltage scan after correction for space-charge potential.

The interesting region of 0–5 eV c.m. energy was thus scanned four times. Four data sets of spectra were recorded in one measuring cycle with different conditions [Fig. 1(a)]. The electron velocity is higher than the ions in the first two spectra and lower than the ion velocity in the latter two spectra. In the middle of the scan there is a point where the electron velocity equals the ion velocity, thus its energy is zero in the c.m. frame. After each cycle a new ion beam was injected into the ring. The data were taken in 3997 complete cycles. Each recorded event consists of the SBD pulse height, the cathode voltage, and a time ramp that is digitized in 7000 steps over the scan range. More details about this scanning method can be found in Ref. [16].

III. THEORETICAL BACKGROUND

A. Calculation of resonances

Accurate predictions of energy positions and widths of doubly excited states can be accomplished with relativistic many-body perturbation theory (RMBPT), see, e.g., Ref. [2] and references therein. Here we use RMBPT in an all-order formulation, the so-called coupled-cluster single- and double-excitation scheme (CCSD) [17], where the full problem is reduced to a coupled two-particle problem. During the formation of DR resonances the $2s_{1/2}$ electron is excited to $2p_j$ where the excitation energy is provided by the binding of a continuum electron. An accurate determination of the $2p_j$-$2s_{1/2}$ splittings in the Be^+ ion is therefore the first step of the calculation of DR resonances. In a second step we calculate the doubly excited states in Be accounting for the interaction between the captured electron and the $1s^2$ core as well as for the interaction with the excited target electron. This latter interaction is decisive for the properties of the doubly excited state and determines not only the position but also the lifetime of the state. Doubly excited states are generally very fragile and decay predominantly by autoionization, i.e., they are embedded in the continuum. To be able to handle this situation, we use the complex rotation method that makes a treatment of decaying states without explicit continuum functions possible. The method directly gives the autoionization width of a resonance as the imaginary part of a complex energy. The many-body perturbation theory combined with complex rotation has been successfully applied in both nonrelativistic [18,19] and relativistic calculations [1,2,7,20]. The third step in the calculation is to calculate the cross section for recombination, which after folding with the relevant electron velocity distribution can be directly compared to experimental recombination spectra. This third step is described in more detail below.

B. Calculation of recombination cross section

To calculate the recombination cross section we use the method previously described in Ref. [21], which has been applied to DR of lithiumlike F^{6+} [21] and copperlike Pb^{53+} [22]. The RR process, Eq. (1), and DR process, Eq. (2), both start with Be^+ in its ground state plus an incoming electron and end with Be in a bound, but possibly excited, state plus a photon. Recombination into this bound state s is the time inverse of photoionization from s, and methods developed for this latter process [23] can be used. For recombination calculations it is natural to write the cross section as a function of electron energy instead of as a function of photon energy. These two quantities are, of course, locked to each other via

$$\hbar\omega = \varepsilon_e + E_{\rm ion} - E_s\,, \tag{3}$$

and the cross section for recombination can be written as

$$\sigma_{ion\to s}(\varepsilon_e) = \frac{1}{g_i}\frac{e^2}{4\pi\epsilon_0}\frac{4\pi}{3}\frac{\omega}{c}\left(\frac{\hbar\omega}{c}\right)^2\frac{1}{2m_e\varepsilon_e} \times {\rm Im}\left\{\sum_n \frac{\langle\Psi_s|\mathbf{r}e^{i\theta}|\Psi_n\rangle\cdot\langle\Psi_n|\mathbf{r}e^{i\theta}|\Psi_s\rangle}{E_n - E_{\rm ion} - \varepsilon_e}\right\}. \tag{4}$$

Equation (4) thus gives the cross section for recombination into a specific bound state s, and it is the basis for the calculated recombination spectra presented here. The total cross section for field-free conditions can be obtained after summation over all bound states s. In storage ring experiments the motional electric fields in the magnets will result in field ionization of weakly bound states (see Sec. V D), and thus not all recombined ions are detected. To describe this, the sum over s has to be truncated appropriately. Every $|\Psi\rangle$ in Eq. (4) represents a correlated many-particle state with complex energy. The sum over n goes over all states, (discretized) continuum states as well as doubly excited states. The presence of the continuum states enables the inclusion of direct radiative recombination. For the doubly excited states the complex energy can be written as $E_n = E_{\rm pos} - i\Gamma/2$. Where $E_{\rm pos} = {\rm Re}\{E_n\}$ determines the resonance position in the cross-section spectra, while $\Gamma = -2\times{\rm Im}\{E_n\}$ is the resonance full half-width. The statistical weight of the initial ion ground state is denoted by g_i, and here $g_i = 2$.

Equation (4) allows for interference between RR and DR since the wave functions $|\Psi_n\rangle$ implicitly include both the so-called bound parts and the open channels. This is a property of the complex rotation method and through the open channels the matrix elements obtain imaginary parts. The real part of such a complex matrix element squared is responsible for the symmetric part of the cross section, while the imaginary part directly introduces an asymmetric behavior. A more detailed discussion can be found in Ref. [24].

The strength of a resonance is a useful concept and is closely related to Eq. (4). It is defined as the integrated cross section due to a particular doubly excited state n. In the case when, for a specific doubly excited state n, the numerator in Eq. (4) has a vanishingly small imaginary part, the contribution from that state takes the form of a Lorentz profile. Integration over ε_e will then give

$$S_n = \int \sigma(\varepsilon_e)\,d\varepsilon_e = \frac{\hbar^3\pi^2}{2m_e\,{\rm Re}\{E_n - E_{\rm ion}\}}\frac{g_n}{g_i}A^r_{n\to s}\,, \tag{5}$$

where $A^r_{n\to s}$ is the radiative transition rate in the dipole approximation, which is in the usual noncomplex rotated way written as

$$A^r_{n\to s} = \frac{1}{g_n}\sum_{M_s,M_n}\frac{e^2}{4\pi\varepsilon_0}\frac{4}{3\hbar}\left(\frac{\omega}{c}\right)^3 {\rm Re}\{\langle\Psi_s^{J_sM_s}|\mathbf{r}|\Psi_n^{J_nM_n}\rangle^2\}. \tag{6}$$

The sum in Eq. (6) goes over all magnetic substates of the two levels n and s, and is averaged over the magnetic substates of the initial state n by division with the multiplicity g_n. An implicit assumption in Eq. (4), and thus in Eq. (5), is that the radiative rate A^r is much smaller than the autoionization rate A^a. In Eq. (5) one can easily correct for this assumption by multiplication with the ratio between the capture rate and the total decay rate. Since all doubly excited states studied here can only autoionize to the ground state of the Be^+ ion, the autoionization rate equals the capture rate. If we also sum over all possible final recombined states s, we find the frequently used formula

$$S_n = \frac{g_n}{g_i}\frac{\hbar^3\pi^2}{2m_e\,{\rm Re}\{E_n - E_{\rm ion}\}}\frac{A^a_n\sum_s A^r_{n\to s}}{A^a_n + \sum_s A^r_{n\to s}}. \tag{7}$$

C. Conversion to rate coefficients

The acceleration of the electrons to an energy of around 700 eV reduces their longitudinal velocity spread. The transverse spread remains unaffected. The electron velocity distribution is described by the so-called ''flattened'' Maxwellian distribution [25],

$$f(\vec{v}_e,\Delta v_e) = \frac{m_e}{2\pi kT_\perp}\sqrt{\frac{m_e}{2\pi kT_\parallel}}\exp\left(-\frac{m_e v_{e\perp}^2}{2kT_\perp} - \frac{m_e(v_{e\parallel}-\Delta v_e)^2}{2kT_\parallel}\right), \tag{8}$$

with $v_{e\perp}$ and $v_{e\parallel}$, respectively, being the perpendicular and parallel components of the electron velocity vector $\vec{v}_e$ with respect to the ion beam direction. The detuning of the longitudinal velocity component of the electrons with respect to the ions is expressed by Δv_e. The velocity spread of the ions is generally negligible due to electron cooling and their heavy mass. The relative motion between the electrons and ions is thus governed only by the velocity spread of the electrons.

The shapes of DR resonances are strongly affected by the electron beam transverse temperature at low energies, while

at high energies the experimental energy resolution $\Delta\varepsilon_e$ is determined by the electron velocity and longitudinal temperature $kT_\parallel$ as [26]

$$\Delta\varepsilon_e = \sqrt{(kT_\perp \ln 2)^2 + 16\, kT_\parallel \varepsilon_e \ln 2} \approx 3.33\sqrt{kT_\parallel \varepsilon_e}. \quad (9)$$

In order to compare the theoretical results with the experimental rate coefficient, it is necessary to fold the calculated cross section with the electron velocity distribution,

$$\alpha_{\text{theor}}(\Delta v_e) = \int d^3\vec{v}_e v_e \sigma(v_e) f(\vec{v}_e, \Delta v_e), \quad (10)$$

which can also be expressed in the relative electron energy scale as $\alpha_{\text{theor}}(\varepsilon_e)$.

IV. DATA ANALYSIS

The aim of the data analysis is to obtain the energy positions and the rate coefficients of the DR resonances from the recorded data. As the cathode voltage is recorded by an analog-to-digital converter as channel numbers, a voltage calibration is needed for conversion of the voltage channels back to the cathode voltage. In this calibration, random events are recorded with the cooler cathode voltage being set to several discrete values throughout the scan range used in the measurements. As the channel number corresponding to each voltage is well defined by the respective peak, the cathode voltage as a function of the channel number is obtained by a fit. Due to the existence of the space charge potential U_{sp}, the real electron energy E_e is related to the cathode voltage U_{cath} by

$$E_e = e(U_{\text{cath}} - U_{\text{sp}}), \quad (11)$$

where U_{sp} is modeling by the following formula [27]:

$$U_{\text{sp}}(v_e) = (1-\zeta)\frac{I r_c m_e c^2}{v_e e^2}\left[1 + 2\ln\left(\frac{b}{a}\right) - \left(\frac{r}{a}\right)^2\right]. \quad (12)$$

Here v_e is the laboratory frame electron velocity, I is electron current, r_c the classical electron radius, r the distance from the electron beam axis, and a and b are the radii of the electron beam and the cooler tube, respectively. The condition $r=0$ is assumed throughout the experiment because the ion beam is only 1 mm in size after cooling and is aligned to the axis of the electron beam. The parameter ζ represents the contribution of the trapped ions, created by electron impact ionization of residual gas molecules, to the space charge potential. The compensation parameter ζ can be determined by inserting the values of the cathode voltage U_{cath} and the electron energy E_e at cooling into Eqs. (11) and (12). The real electron velocity can be derived from the ion velocity at cooling from the Schottky frequency and the length of the ion orbit C in the ring. Besides the corrections for the space-charge potential, another correction needs to be made. Figure 1(b) shows the spectrum that results from the cathode voltage scan before (gray line) and after (black line) the space-charge potential correction, that produces a shift of ≈ 0.9 eV in the c.m. frame. During the scan, when the average electron velocity and ion velocity differ, the interaction between them tends to drag the ions. The change of the ion energy during the cathode voltage scan was found to correspond to a change in the electron energy (in laboratory frame) of 1 eV, which corresponds to approximately 0.4 meV in the c.m. system.

For transformation of the energy from the laboratory frame to the c.m. frame, the space-charge-corrected electron energy E_e, and the drag-force-corrected ion energy E_i for each data point are inserted in the relativistic formula,

$$\varepsilon_e = -(m_i+m_e)c^2 + [\{E_i + E_e + (m_i+m_e)c^2\}^2 - (\sqrt{E_i^2 + 2m_i c^2 E_i} + \sqrt{E_e^2 + 2m_e c^2 E_e})^2]^{1/2}. \quad (13)$$

In the following paragraph we are going to discuss different contributions to the uncertainty in c.m. energy ε_e. First, as seen above, the overall changes in the ion energy do not contribute to the uncertainty in the c.m. energy. There are two contributions to the uncertainty which are important: the dominant one is due to the conversion of the voltage channel to the cathode voltage and the second one is due to the space-charge correction. The uncertainty in the conversion from the voltage channel to the cathode voltage gives a maximum error of ± 13 meV at 5 eV in the c.m. system. This error propagates over the entire c.m. energy scale with a relative error of 0.26%. As said earlier, the calculation of the space-charge correction depends critically on the well-defined velocity of the electrons and ions at the cooling conditions and on the approximate calculation of the compensation parameter ζ. In the first case the uncertainty in the length of the ion beam orbit, which is 3 cm, produces an uncertainty of ± 7 meV in the c.m. energy. The ζ parameter was found to be rather small, 0.045. The potential raised by the electron beam is calculated to be approximately 50 V, which means that the potential from the trapped positive ions is approximately 2 V or 1 meV in the c.m. system. Thus the uncertainty in ζ gives a negligible contribution to the overall error in the c.m. system. We should point out that the changes in the ion energy during the cathode voltage scan could be disregarded. Finally, we arrive at the maximum error in the c.m. energy of 18 meV or a relative error of 0.4% over the entire energy scale.

In order to determine the resonance strengths from the spectra, the numbers of detected ions were converted to the rate coefficients by

$$\alpha_{\text{expt}}(\varepsilon_e) = \frac{R_t \gamma^2}{N_i n_e l / C}, \quad (14)$$

where $R_t = N_{\text{ct}}/(\Delta t\, N_{\text{cyc}})$ is the background-subtracted count rate, N_{ct} is the number of counts in the tth time channel, Δt is the time interval per channel, N_{cyc} is the number of data taking cycles, $\gamma = [1-(v_i/c)^2]^{-1/2}$ is the Lorentz factor, N_i is the number of ions stored in the ring, and n_e is the electron density. The main contributions to the background in the measured rate coefficient come from electron capture from the residual gas. The background was treated as a constant. It can be derived by simply averaging the rate over c.m. energy range (0.5–1 eV) where there are no DR contributions and

TABLE I. The contributions to the $2s_{1/2}$, $2p_{1/2}$, and $2p_{3/2}$ energies (relative to Be^{2+}) and to the $2p_j$-$2s_{1/2}$ splittings in the Be^+ ion. The numbers in the first three columns are given in atomic units for ^{9}Be, i.e., 1 a.u.$=27.211\,383\,4\,M/(M+m_e)$ eV$=27.209\,727\,1$ eV. Uncertainties in shown numbers are enclosed in parentheses.

	$2s_{1/2}$ (a.u.)	$2p_{1/2}$ (a.u.)	$2p_{3/2}$ (a.u.)	$2p_{1/2}$-$2s_{1/2}$ (eV)	$2p_{3/2}$-$2s_{1/2}$ (eV)
Dirac-Fock	−0.666183	−0.519447	−0.519406	3.9927	3.9938
ΔDirac-Fock-Breit	0.000024	0.000023	0.000009	0.0000	−0.0004
Mass polarization	0.000000	−0.000016	−0.000016	−0.0004	−0.0004
Coulomb-Coulomb correlation					
Second-order core-valence					
$\ell_{max}=4$	−0.003905	−0.004120	−0.004117		
$\ell_{max}=5$	−0.003915	−0.004144	−0.004141		
$\ell_{max}=6$	−0.003920	−0.004155	−0.004152		
$\ell_{max}=7$	−0.003923	−0.004160	−0.004158		
$\ell_{max}=8$	−0.003925	−0.004164	−0.004161		
Extrapolated	−0.003929(2)	−0.004170(3)	−0.004168(3)	−0.0066	−0.0065
Second-order core-core	0.000996	0.000253	0.000253	−0.0202	−0.0202
Higher order	−0.000186	−0.000422	−0.000421	−0.0064	−0.0064
Coulomb-Breit correlation					
Second-order core-valence	−0.000008	−0.000003	−0.000002	0.0001	0.0002
Second-order core-core	0.000002	0.000001	0.000001	0.0000	0.0000
Total RMBPT[a] (CCSD)	−0.669284(10)	−0.523780(20)	−0.523751(20)	3.9591(6)	3.9599(6)
Ref. [28][b] CCSD	−0.669304	−0.523804	−0.523774		
Ref. [28][b] + some effects beyond CCSD	−0.669293(3)	−0.523786(6)	−0.523756(6)	3.9592(2)	3.9600(2)
Experiment[c]	−0.6692883(2)	−0.523801(1)	−0.523771(1)	3.95866(3)	3.95948(3)

[a]The uncertainty is dominated by a rough estimate of uncalculated effects beyond CCSD (see text).

[b]The values for the binding energies reported in Ref. [28] (given in a.u. for infinite nuclear mass) are here divided by a factor $R_{Be}/R_\infty = 0.999\,939\,132$, in order to compare with the present result.

[c]Hollow-cathode discharge emission spectroscopy. Reference [30] gives the binding energies of $Be^+(2s_{1/2})=146\,882.86(5)$ cm^{-1}, $Be^+(2p_{1/2})=114\,954.10$ cm^{-1}, and $Be^+(2p_{3/2})=114\,947.52$ cm^{-1}. The values presented in the table are obtained from division by twice the Rydberg constant for beryllium ($R_{Be}=109\,730.63$ cm^{-1}).

the RR rate is negligible. The uncertainty in the measured rate coefficient was conservatively estimated to be 21%, mainly due to the uncertainty in the ion current measurement and in the length of interaction region.

V. RESULTS AND DISCUSSION

A. Calculation of energy levels in the Be^+ ion

The contributions to the binding energies of the $2s_{1/2}$, $2p_{1/2}$, and $2p_{3/2}$ states in Be^+, together with the $2p_j$-$2s_{1/2}$ splittings are given in Table I. The first row gives the Dirac-Fock contribution, while the second shows the effects due to the Breit interaction when it is added to the Dirac-Fock Hamiltonian. The retardation beyond the Breit interaction is in the lowest order less than 1×10^{-9} a.u. and is thus of no significance for the number of figures shown in Table I. The nuclear size effect is also too small to be seen with the precision displayed in Table I. The third row shows the lowest-order mass polarization. It contributes to the $2p_j$ states only since the ground state, containing only s electrons, is not affected in first order. To underline the importance of correlation, to high orders, the Coulomb correlation contribution has been divided into second-order contribution, and the all-order CCSD result. The partial-wave expansion is carried on until $\ell_{max}=8$ and extrapolated from there. In the second order only the core-valence correlation is affected by the infinite sum over partial waves. We estimate the uncertainty in this part as half the extrapolation contribution. The Coulomb-Breit correlation, resulting from one order in the Coulomb and one in the Breit interaction correlation, is in this light system three orders of magnitude smaller than the pure Coulomb correlation and is just calculated in second order [27].

Blundell *et al.* [28] have earlier performed an all-order relativistic calculation on the $2\ell_j$ energies in Be^+. This calculation is also using the CCSD approximation, but is adding some extra effects, see below. The calculation is in fact very similar in spirit to our calculation. The agreement is also close, but not perfect. One difference is that the Ref. [28] starts from a Dirac-Fock basis set, instead of a Dirac-Fock-Breit basis set, but this is rather unimportant in such a light system as Be^+. In fact the sum of all contributions involving the Breit interaction agrees to within $\sim1\times10^{-6}$ a.u. Another difference is in the partial-wave expansion which stops at

TABLE II. A breakdown of the contributions which determines the positions of some of the low-energy Be($2p_j 3\ell_{j'}$) resonances (eV).

	$2p_{1/2}3s_{1/2}$ $J=0$	$2p_{3/2}3p_{3/2}$ $J=3$	$2p_{3/2}3d_{5/2}$ $J=4$
$(2p_j-2s_{1/2})+$ Dirac-Fock-Breit description of $3\ell_{j'}$	1.3867	1.9765	2.4401
Coulomb correlation of $1s^2$ with $3\ell_{j'}$	−0.0036	−0.0033	−0.0004
Full $2p_j 3\ell_{j'}$ correlation	−0.0994	−0.1290	−0.1216
Total	1.2837	1.8442	2.3182

$\ell_{\max}=6$ in Ref. [28] and at $\ell_{\max}=8$ here. In both cases the result is, however, extrapolated to infimum and the uncertainty in this procedure should definitely be within a few parts in 10^{-6} a.u. The CCSD result from Ref. [28] is still $\sim 20\times 10^{-6}$ lower than the present result and the reason of this is not clear to us. The difference is, however, rather similar for all the $2\ell_j$ energies and affects the $2p_j$-$2s$ energy splittings much less. In Ref. [28] also some effects beyond the CCSD result were considered [called $E(3)$-extra]. The result including the $E(3)$-extra contributions is listed separately in Table I and agrees much better with our calculation, but that can only be a coincidence. The $E(3)$-extra contributions can be obtained with results available at the CCSD level, but belongs formally to the triply excitation scheme. Salomonson and Ynnerman have shown that there are important cancellations at this level [29] and the size of the $E(3)$-extra contributions has been used here as a rough estimate of the uncertainty due to uncalculated effects. The uncertainty then equals 5% of the higher-order correlation contributions.

Very accurate emission spectroscopy measurements exist for Be^+ [30]. The uncertainties for the energy positions of the $2p_j$ states and of the $2p_j$-$2s$ energy splittings given in Table I are obtained as recommended in Ref. [31]. The calculated results agree with the measurements within the error bars discussed above.

B. Resonances in the Be atom

In order to determine the positions of the resonances in the recombination rate coefficient the interaction between the captured electron and the excited target ion has to be calculated, as discussed in Sec. III A. Table II shows the contributions that determine the position for some of the low-energy resonances. For simplicity, only the states that, due to symmetry reasons, are dominated by one jj configuration are shown. The first line gives the resonance position when the outer, $3\ell_{j'}$, electron interacts with the $1s^2$ core through a Dirac-Fock-Breit potential. The second line contains the corrections coming from the correlation between the $3\ell_{j'}$ electron and the $1s^2$ core. The fully correlated description of the $2p_j 3\ell_{j'}$ interaction (third line) accounts for both Coulomb and Breit correlation, but the latter is insignificant.

We have calculated in total 250 doubly excited states in the Be atom which are placed above the first and below the second ionization limit. Table III gives resonance positions, widths, A^a, A^r, and DR strengths of the first 26 resonances of the $(2p_{1/2,3/2}3\ell_j)_J$ doubly excited states. But all results for resonances up to $(2p_{1/2,3/2}7\ell_j)_J$ are used in Fig. 2. All calculations, being fully relativistic, are naturally performed in the jj coupling scheme. In order to understand the character of the resonances they are projected onto an LS-coupled basis. The second column of Table III displays the dominant LS term with its weight and it is clear that most resonances, as expected, are well described in the LS-coupling scheme. However, in a nonrelativistic calculation eight of the resonances would not exist, since the $2p3p\ ^{1,3}P$ and $2p3d\ ^{1,3}D$ symmetries cannot autoionize in pure LS coupling. The spin-orbit-induced admixture of other L symmetries, S or D and P or F, respectively, causes these states to be weakly autoionizing, with up to six orders of magnitude slower rates compared to those that can autoionize nonrelativistically. The branching ratios, $A^a/(A^a+A^r)$, see Eq. (7), for these nonrelativistically forbidden resonances range from 0.52 to 0.95, and consequently reduce the corresponding recombination strengths by at most 48% (in the case of the $2p3d\ ^3D_1$ resonance). Several of these nonrelativistically forbidden resonances also give substantial contributions to the rate coefficient, see, e.g., the $2p3d\ ^3D$ resonances in Table III and Fig. 3. The $2p3p\ ^1P$ (forbidden) resonance is quite isolated in the spectrum and can be clearly identified in Figs. 2 and 3.

The calculated resonance positions in the recombination cross section are displayed in the third column of Table III and are in good agreement with the available (see Ref. [31]) experimental data, given in the fourth column. The agreement is usually far better than 5 meV. The only exception is the broad $^1P_1$ resonance at 1.59 eV where the disagreement in position is 16 meV. This is, however, a very broad resonance, with an autoionization width of nearly 0.5 eV, and where thus the experimental energy position [32] should be taken with less confidence, as has been noticed also in Ref. [31].

C. Overview of the spectra

The experimental recombination rate coefficient of lithiumlike Be^+ is shown in Fig. 2. Besides the strong rise of the rate coefficient near zero c.m. energy, the spectrum contains the $\Delta n=0$ DR resonances due to the occurrence of $2s_{1/2} \rightarrow 2p_j n\ell$ excitations. The lowest-energy resonance is due to the $(2p^2)\ ^1S_0$ doubly excited state [33]. The shapes of DR resonances are strongly affected by the electron beam transverse temperature at low relative energies. At high energies the width of the resonances is related to the longitudinal temperature by Eq. (9), which we use to obtain the initial value $(kT_\parallel)_{\rm init}=0.17$ meV for the longitudinal temperature by Gaussian fit of the experimental rate coefficient at 1.28 eV energy. The optimal values of $kT_\perp=1$ meV and $kT_\parallel=0.22$ meV were found after fitting the experimental rate coefficient at the same energy range around 1.28 eV, but using the proper model for the rate coefficient given by Eq.

TABLE III. Positions, widths, and strength for the lowest Be$(2p_j\, n\, \ell_{j'})_J$ resonances in the recombination cross section. The dominating jj and LS terms along with the extends to which they describe the state are given in the first and second column, respectively. The autoionization rate is denoted by A^a and the radiative rate with A^r. The resonance strengths are calculated according to Eq. (7). Numbers enclosed in brackets are powers of 10.

Configuration (to %)		Position: $E_{\rm pos}$-$E_{\rm ion}$ (eV)		This work: calculation only			
jj term	LS term	This calc.	Ref. [31]	Width: Γ (eV)	A^a (ns^{-1})	A^r (ns^{-1})	Strength: S_n (10^{-22} eV cm^2)
$(2p^2)$	$^1S_0$ [a]	0.1241	0.123	9.251[−3]	14055.94	0.220	21.92
$(2p_{1/2}3s_{1/2})_0$ 97%	$^3P_0$ 99%	1.2837	1.2847	1.793[−4]	272.44	0.193	1.85
$(2p_{1/2}3s_{1/2})_1$ 65%	$^3P_1$ 88%	1.2840	1.2849	1.802[−4]	273.76	0.192	5.54
$(2p_{3/2}3s_{1/2})_2$ 97%	$^3P_2$ 99%	1.2845	1.2854	1.799[−4]	273.27	0.194	9.32
$(2p_{3/2}3s_{1/2})_1$ 78%	$^1P_1$ 88%	1.5931	1.577[b]	4.890[−1]	742980.45	1.038	24.18
$(2p_{3/2}3p_{3/2})_1$ 55%	$^1P_1$[c] 53%	1.7323	1.7269	2.1[−7]	0.32	0.096	1.58
$(2p_{1/2}3p_{1/2})_1$ 73%	$^3D_1$[d] 40%	1.8435		1.202[−3]	1825.87	0.166	3.34
$(2p_{1/2}3p_{3/2})_2$ 49%	$^3D_2$[d] 100%	1.8438		1.200[−3]	1823.05	0.164	5.49
$(2p_{3/2}3p_{3/2})_3$ 98%	$^3D_3$[d] 100%	1.8442		1.197[−3]	1818.23	0.169	7.92
$(2p_{3/2}3p_{1/2})_1$ 29%	$^3S_1$[d] 63%	2.0208	2.0189[e]	1.119[−2]	17002.71	0.285	5.24
$(2p_{1/2}3p_{1/2})_0$ 67%	$^3P_0$[c] 99%	2.0857	2.0857	1.01[−6]	1.54	0.133	0.72
$(2p_{1/2}3p_{3/2})_1$ 50%	$^3P_1$[c] 99%	2.0858	2.0858	6.6[−7]	1.00	0.138	2.16
$(2p_{3/2}3p_{3/2})_2$ 67%	$^3P_2$[c] 89%	2.0861	2.0861	1.64[−6]	2.49	0.138	3.87
$(2p_{3/2}3p_{1/2})_2$ 33%	$^1D_2$ 89%	2.1126		1.032[−1]	156817.99	0.217	6.36
$(2p_{3/2}3d_{5/2})_2$ 46%	$^1D_2$[c] 57%	2.2526	2.2567	1.220[−6]	1.85	0.114	2.95
$(2p_{1/2}3d_{3/2})_2$ 75%	$^3F_2$ 32%	2.3176		1.528[−1]	232120.70	0.248	6.61
$(2p_{3/2}3d_{3/2})_3$ 53%	$^3F_3$ 92%	2.3178		1.528[−1]	232115.66	0.233	8.69
$(2p_{3/2}3d_{5/2})_4$ 100%	$^3F_4$ 100%	2.3182		1.528[−1]	232110.28	0.251	12.05
$(2p_{1/2}3d_{3/2})_1$ 50%	$^3D_1$[c] 85%	2.3543	2.3552	1.13[−7]	0.17	0.154	1.28
$(2p_{3/2}3d_{3/2})_2$ 53%	$^3D_2$[c] 61%	2.3544	2.3553	1.11[−6]	1.68	0.159	3.83
$(2p_{3/2}3d_{5/2})_3$ 71%	$^3D_3$[c] 76%	2.3545	2.3554	1.58[−6]	2.40	0.168	5.79
$(2p_{3/2}3p_{3/2})_0$ 59%	$^1S_0$ 100%	2.4486		8.979[−3]	13642.53	0.339	1.71
$(2p_{1/2}3d_{5/2})_2$ 45%	$^3P_2$ 58%	2.4796		1.296[−2]	19689.34	0.310	7.74
$(2p_{3/2}3d_{3/2})_1$ 50%	$^3P_1$ 94%	2.4799		1.296[−2]	19686.58	0.296	4.43
$(2p_{3/2}3d_{3/2})_0$ 93%	$^3P_0$ 100%	2.4800		1.295[−2]	19677.18	0.312	1.55
$(2p_{1/2}3d_{5/2})_3$ 33%	$^1F_3$ 72%	2.5076		8.719[−2]	132466.32	0.299	10.32
$(2p_{3/2}3d_{5/2})_1$ 56%	$^1P_1$ 75%	2.5375	2.536	1.831[−4]	278.17	0.298	4.36

[a]Resonance position, width, and autoionization rate are extracted from nonrelativistic calculations of Ref. [33].
[b]Nonrelativistically forbidden.
[c]Resonance with interference effects.
[d]The autoionization width of this resonance is very broad, which affects the reliability of the experimentally determined energy position.
[e]Originally (Ref. [50]) assigned to $2s2p\ ^3P^o$-$2p3p\ ^3D^e$ transition, and reassigned in Ref. [51] to $2s2p\ ^3P^o$-$2p3p\ ^3S^e$ transition.

(10). On the other hand, the expected value of the longitudinal temperature is 0.1 meV which is given by [25]

$$T_{\parallel}=\frac{kT_{\rm cath}^2}{4E_{\rm cool}}+\left(\frac{2m_ec^2r_{\rm c}}{k}\right)\left(\frac{4\pi n_e}{3}\right)^{1/3}, \qquad (15)$$

where $T_{\rm cath}$ is the cathode temperature (1173 K), $E_{\rm cool}$ is the electron cooling energy, $r_{\rm c}$ is the classical electron radius, and n_e is electron density. The difference between the expected longitudinal temperature and the optimal value obtained by fitting may be due to a slight displacement of the ion beam from the center of the electron beam.

Since the energy splitting between the $2p_{3/2}$ and $2p_{1/2}$ states is very small for this light element ($\approx 8.16\times10^{-4}$ eV) [34], just one Rydberg series of DR resonances corresponding to an excitation of a $2s$ electron to $2p$ is visible (see Fig. 2).

As shown in Figs. 2 and 3 the theory achieves good agreement with the experimental data with respect to resonance positions (for details see Tables III and IV). In Table IV we compare some of the lowest experimental and calculated resonance positions. An agreement to within 4 meV is obtained for the groups of resonances shown here, but the experimental resolution is insufficient to uncover the fine structure. In order to make this comparison, the energy positions were obtained by the same fit to the experimental and calculated resonance groups. If one compares the calculated positions of the same resonances in the cross section with the rate

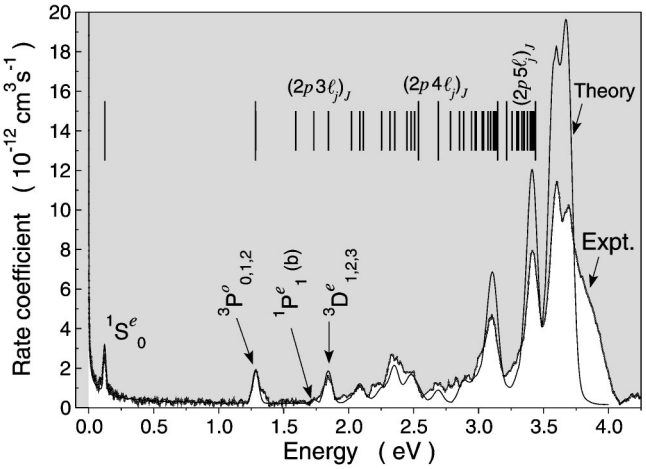

FIG. 2. The white area shows the spectrum obtained by combining the four spectra from the measurement with the electron current $I=31$ mA. The calculated cross section with $n_{\mathrm{cutoff}}=7$, convoluted with $kT_{\perp}=1$ meV and $kT_{\parallel}=0.22$ meV (for details see text), is shown by the thin solid line. The $^1P^e_1$ state at 1.7 eV [labeled with (b)] is an example of nonrelativistically forbidden resonance that is quite isolated and therefore clearly visible.

coefficient (see Table III), one can see a small shift towards lower energies which is due to the folding procedure [see Eq. (10)].

Concerning the size of the rate coefficient, one notices that the theory is a factor of up to 1.7 higher than the experimental one in the high-energy region ($\varepsilon_e>3$ eV). Whereas at energies $\varepsilon_e\leqslant 3$ eV, theory and experiment are in good agreement also in absolute height (see Fig. 3). This mismatch is thus not due to a systematic error in the normalization for obtaining absolute rate coefficients.

Very close to the second ionization threshold of Be, the observed DR rate coefficient is influenced by the removal of

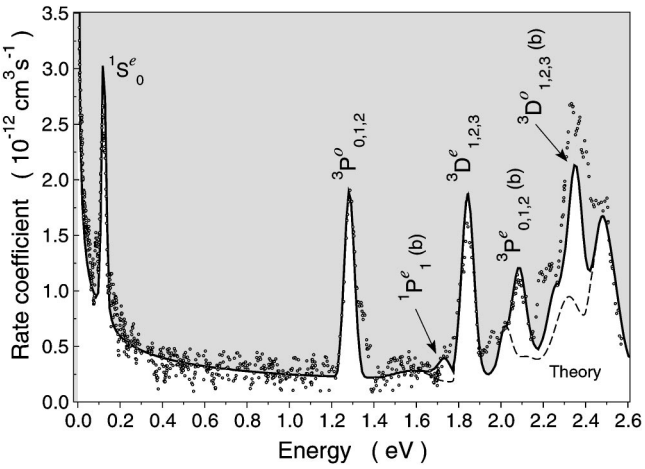

FIG. 3. A detailed view of the low-energy region in the DR spectrum showing the resonances listed in Table III. The experimental data is shown as dots while the calculation is given by the white area under the thick solid line. Resonances labeled with (b) are nonrelativistically forbidden, and their exclusion from the cross section will result in somewhat lower rate coefficients shown as a dashed line.

TABLE IV. A breakdown of the positions of the lowest prominent resonances in the recombination rate coefficient observed in this experiment and compared with the present calculations. Uncertainties are in parentheses.

Resonances	Expt. (eV)	Calc. (eV)
$(2p^2)\,^1S_0$	0.119(7)	0.1208
$(2p\,3s)^3P_{0,1,2}$	1.287(9)	1.2835
$(2p\,3p)^3D_{1,2,3}$	1.842(9)	1.8432

the weakly bound Rydberg electron due to field ionization in the bending (main dipole) magnet. A rough estimate for the principal quantum number n_{cutoff} above which the Rydberg electrons are no longer bound is given by [35]

$$n_{\mathrm{cutoff}}=\left(6.2\times 10^{10}\frac{q^3}{v_i B}\right)^{1/4}, \tag{16}$$

where q is the charge state of the ion and B is the magnetic flux density in the dipole magnet. For the ion velocity $v_i=0.049\,85(3)\times c$ and $B=1.16$ T used in this experiment, one arrives at an $n_{\mathrm{cutoff}}\approx 7$. Therefore, it is expected that contributions to resonances will be greatly reduced for states with $n\geqslant 8$. Since the reionized recombined systems cannot contribute to the measured rate, ''hard cutoff'' $n_{\mathrm{cutoff}}=7$ is introduced in the theoretical calculations, see Eq. (4). The theoretical rate coefficient in Fig. 2 was obtained for this condition.

D. Effects due to external fields

A preliminary investigation of field ionization features of Be Rydberg states is summarized in Fig. 4. In Fig. 4(a) we present our calculations of the Stark structure of the Be energy levels. The energies were calculated by direct diagonalization (with manifolds up to $n=12$ included) for increasing field strengths (200 V/cm increment) and the energy level plot was generated by connecting the eigenvalues, using third-order spline interpolation between the field points. To compute the matrix elements of the dipole moment, we used the nonhydrogenic formulas given by Ryde [36]. By examination of the zero field binding energies for the Be atom [31], one can find a strong perturbation of the Rydberg series, where the $(2s\,nd)\,^1D$ levels are above all $(2s\,nF,G,H,I)$ levels due to influence of a $2p^2$ perturber on the $s\,d$ series [37–40]. This effect causes the $(2s\,nd)\,^1D$ levels to have appreciable negative quantum defects [39] and to shift quadratically (along with $2s\,n\,^{1,3}S$, $^{1,3}P$, and ^3D series) at low field strengths. In this regime $(2s\,nF,G,H,I)$ the levels of each manifold suffer linear energy shifts that form a pseudohydrogenic Stark fan. The field strength in the correction dipole magnet is capable of mixing the high-ℓ subsets with the lower-ℓ (particularly with $^{1,3}D$) members within the $n\geqslant 6$ manifolds. Moreover, the field strength in the main dipole magnet is responsible for overlapping the adjacent $2s\,n\geqslant 6$ Stark manifolds. To calculate the survival probability for each Rydberg state, we used a method introduced in Ref. [35]. The results are summarized in Fig. 4(b). In obtain-

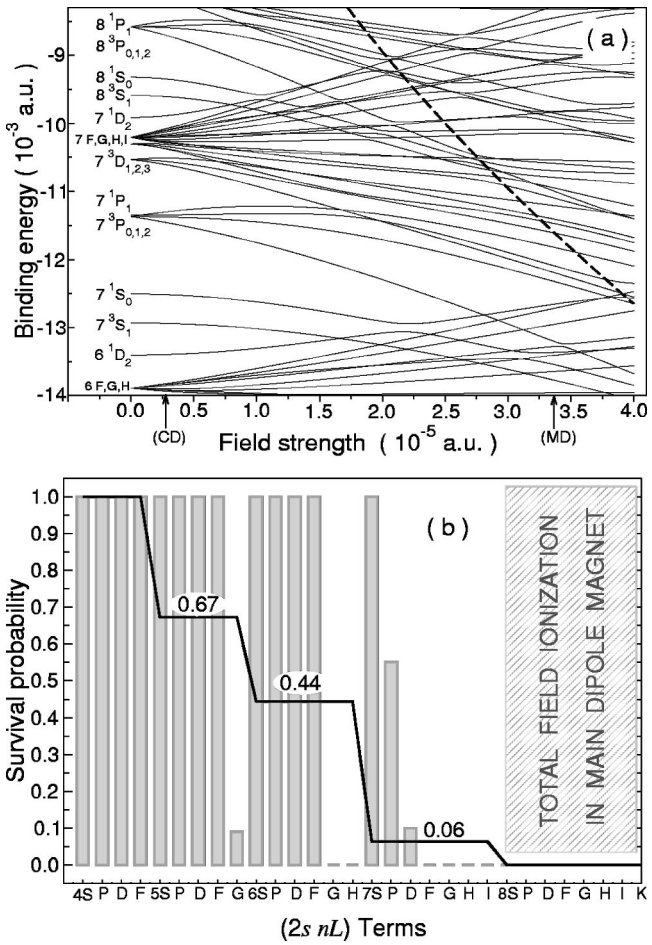

FIG. 4. (a) Stark map of $M_J=0$ Rydberg levels for the manifold $2s\,7L$ in Be. The dashed curve is the classical ionization limit. Vertical arrows on the field strength axis mark the maximum field strength in the correction dipole and main dipole magnets. An atomic unit for the motional electric field strength is $\approx 5.142\,17\times 10^{11}$ V/m. (b) Survival probability of Be excited states after passing through the main dipole magnet. The bars represent statistically averaged (over all possible values of M_J and J quantum numbers) survival probabilities; variation in the field strength along the ion beam axis is included as in Ref. [35]. The solid line gives a description of L-averaged survival probabilities for each of the manifolds considered.

ing statistically averaged survival probabilities we assumed that states whose absolute values of the quantum defect are less than 0.01 will follow diabatic paths having field-dependent lifetimes calculated by Damburg and Kolosov [41,42]. All other Stark levels of the same M_J value will mutually repel (e.g., all the avoided crossings are traversed adiabatically) and will be completely ionized if they reach the classical ionization limit. Within such a simplified model, the solid line in Fig. 4(b) describes L-averaged survival probabilities for each manifold. This confirms the result of Eq. (16) that the states with $n\geqslant 8$ cannot contribute to the recombination rate. In addition, all $(2s\,6G,H)$ and $(2s\,7F,G,H,I)$ states will be also destroyed during the flight through the main dipole magnet with a dwell time of ≈ 30 ns. Taking into account the results shown in Fig. 4(b), we can significantly reduce the disagreement (see Fig. 2) between theoretical and experimental rate coefficients for $(2p\,5\ell)$, $(2p\,6\ell)$, and $(2p\,7\ell)$ resonances. Also, the experimental spectrum displayed in Fig. 2, shows substantial resonance strengths beyond the $2p_j\,n_{\rm cutoff}$ limit. This ''shoulder'' in the experimental rate coefficient can be explained as follows. The distance between the center of the cooler and the dipole magnet is about 1.6 m and the ions have a flight time of ≈ 107 ns. Before the recombined ions reach the main dipole magnet, they pass through toroid and correction magnets where the maximum values of the magnetic flux density are $B=0.03$ T and $B=0.09$ T, respectively. The corresponding motional electric field in the correction magnet is thus capable, according to Eq. (16), of field ionizing the Rydberg states in $\mathrm{Be}^*(1s^2 2s_{1/2} n'\ell'_{j'})$ with $n'\geqslant 16$. Therefore some of the singly excited states $\mathrm{Be}^*(1s^2 2s_{1/2} n'\ell'_{j'})$ with $n_{\rm cutoff}<n'\leqslant 15$ may decay radiatively into the states with principal quantum number $\leqslant n_{\rm cutoff}$ before reaching the dipole magnet. Evidence of this kind of decay has been observed in Refs. [4,19,43], and is known as ''delayed cutoff.'' This conclusion is also supported by Ref. [44], where calculated field-free radiative lifetimes for selected excited states of Be are given. According to those results, $(2s\,nd)\,{}^{1,3}D$ $(n\leqslant 8)$ states have radiative lifetimes less than 100 ns. Due to intramanifold field-induced level mixing in the correction dipole magnet, we can expect considerable reduction in radiative lifetimes of the majority of high-ℓ states within each of the $7\leqslant n\leqslant 15$ manifolds. A more elaborate investigation on this subject is in progress.

E. Recombination at low energy

There are no DR resonances below 0.1 eV, and the high rate coefficient close to zero relative energy is due to nonresonant recombination. The measured rate coefficients are in good agreement with theory for relative energies larger than 10^{-3} eV. This again indicates that our systematic error in the absolute height of the measured rate coefficient is smaller than the estimated 21%. At energies below 10^{-3} eV the measured recombination rate is clearly enhanced and reaches an enhancement factor of 3.1, as seen in Fig. 5.

Enhancements in this energy regime have been found previously in many other measurements using a broad range of bare ions D^+, He^{2+}, N^{7+}, Ne^{10+}, and Si^{14+} [45]. There the enhancement factors were ranging from 1.6 to 3 and the excess in the rate was found to scale with the nuclear charge as $Z^{2.8}$. Li-like ions follow the same trend as has been shown in several experiments, e.g., in Ne^{7+} [4], C^{3+} [46], and argonlike Ti^{4+} [47].

There is evidence that this enhancement of the rate coefficient is caused by the magnetic fields present in the electron cooler [48,49], but the reason for the enhancement is still a subject of ongoing research. We will not discuss this question further here, but note that the excess in the rate found here is $\Delta\alpha=\alpha_{\rm expt}-\alpha_{\rm theor}=20.5\times 10^{-12}$ cm^3 s^{-1}. By determining an effective nuclear charge $Z_{\rm eff}$ value and using the scaling behavior of the rate coefficient with the electron beam temperature, we observe that the size of the excess in

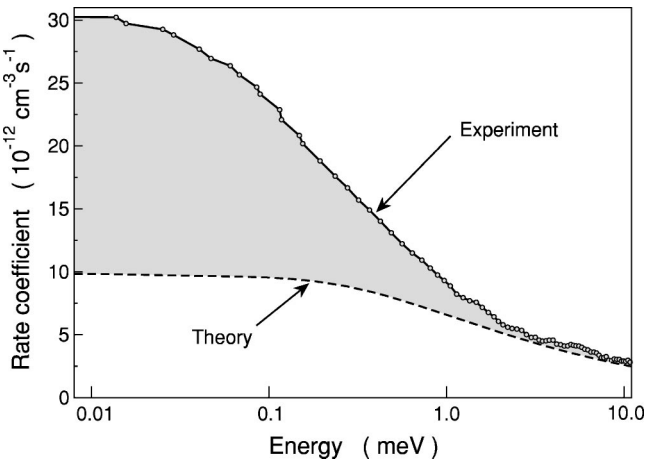

FIG. 5. Comparison of measured and calculated rate coefficients for recombination of Be^+ below 10 meV relative energy. The rate coefficients in this region are determined by nonresonant recombination (RR).

the rate coefficient found here is in accordance with that found earlier with bare ions.

F. Search for the interference effects

As discussed in Sec. III B above, Eq. (4) accounts for interference between DR, Eq. (2), and RR, Eq. (1). The physical background is that the two pathways to recombination may have the same initial and final state. They are then indistinguishable and their amplitudes will interfere quantum mechanically. Such interference leads to asymmetric line shapes of the resonances in the recombination cross section. For this effect to be observable, the two processes must have comparable recombination amplitudes at a given energy. It is not trivial to find a system where this is the case. First the RR rate drops rapidly with increasing relative energy, while DR is usually large only near specific resonance energies. Second, the RR rate is dominated by recombination to the ground state, the rate scales as $1/n$, while most DR resonances recombine predominantly into excited state, reachable by a one electron transition from the doubly excited state. Third, the natural width of the doubly excited state has to be broad enough that its envelope can be followed, i.e., it should be substantially broader than the energy spread of the electron beam. An important additional obstacle is that in the type of experiments reported here, all channels leading to recombination are summed up. Even when asymmetric line profiles do exist, they are often masked by other overlapping resonances.

In Be the lowest-energy resonances have similar principal quantum numbers. The electrons can then interact strongly, leading to several broad resonances, where it might be possible to observe the natural shape of the resonance. Further photostabilization of these resonances is only possible to rather modestly excited states, of the type $2s3\ell_j$ or $2s2\ell_j$, to which the amplitude for direct recombination should still be of nonvanishing size. Early observations [32,50] of beryllium's ultraviolet photoabsorption spectra, and calculations of its photoionization cross section [51], indicated that interference effects should exist for $(2p3p)\,^3D^e$ and $(2p3p)\,^3S^e$ states. Beryllium is therefore an interesting candidate for a search for interference effects in recombination.

When examining the calculated cross sections we find a few asymmetric resonance. As illustrated in Fig. 6(a), there is a clear difference between the full asymmetric cross section and the symmetric part. The full asymmetric cross section is calculated directly from Eq. (4), while the symmetric part is calculated from the real part of its numerator as discussed in Sec. III B.

Interference effects exist unambiguously for the three $(2p_j3p_{j'})\,^3D_J$ resonances around 1.84 eV and less obvious for the $(2p_j3p_{j'})\,^3S_1$ resonance around 2.02 eV. Unfortunately, the asymmetric resonances sit on the wings of some quite broad resonances, $^1P_1^o$ and $^1D_2^e$, which somewhat masks the effect. Figure 6(b), shows the cross section for the three overlaping fine-structure components of $(2p_j3p_{j'})\,^3D_J$ separately, and Fig. 6(c) shows the cross section for three different final states for the $(2p_j3p_{j'})\,^3S_1$ state. The dominating recombination pathway is in all cases to the $(2s3p_{j'})\,^3P_J$ states which is low enough in energy to be populated, to some extent, by radiative recombination. We would like to point out that the photostabilization channel to $(2s\,2p)\,^3P_J$, which is the lowest-energy state with odd parity in Be, would demonstrate very strong interference features [see curve 3 on Fig. 6(c)], but the strength of this channel is several orders of magnitude weaker and it is indeed effectively masked by the channels leading to $(2s3p_{j'})\,^3P_J$ states.

In order to compare the theoretical results with experiments, it is necessary to fold the calculated recombination cross sections with the velocity distribution of the electrons, see Eq. (10). Here we used velocity distributions corresponding to $kT_\perp = 1$ meV and $kT_\parallel = 0.22$ meV. The results for asymmetric and symmetric rate coefficient spectra are presented in Fig. 7(a), showing that the interference effects are smeared out due to the folding procedure. Figure 7(b) represents the relative difference, $(\alpha_{\rm sym} - \alpha_{\rm asym})/\alpha_{\rm sym}$, in the rate coefficient showing that the significance level of the interference effects is at most 10%. The experimental recombination spectrum reported here does not exhibit evidence for asymmetric line shapes. Our statistical error, particularly due to background corrections, is too high. A higher resolution would help, but also a measurement with lower statistical error could reveal the effect.

VI. CONCLUSION

We report experimental and theoretical recombination rate coefficients for Be^+ ions, in both absolute energy and height scales. The calculated rate coefficients for the $\Delta n = 0$ dielectronic resonances show good agreement with experiment for low energies, i.e., well below the series limit. It is noted that the theoretical resonance's strengths at high energies are up to a factor of 1.7 higher than the measured strengths, and we discuss external field effects on the DR rate as the most probable cause. The nonresonant, direct radiative recombination rate is well described by the theory for energies $>10^{-3}$ eV. At a very low electron-ion relative energy,

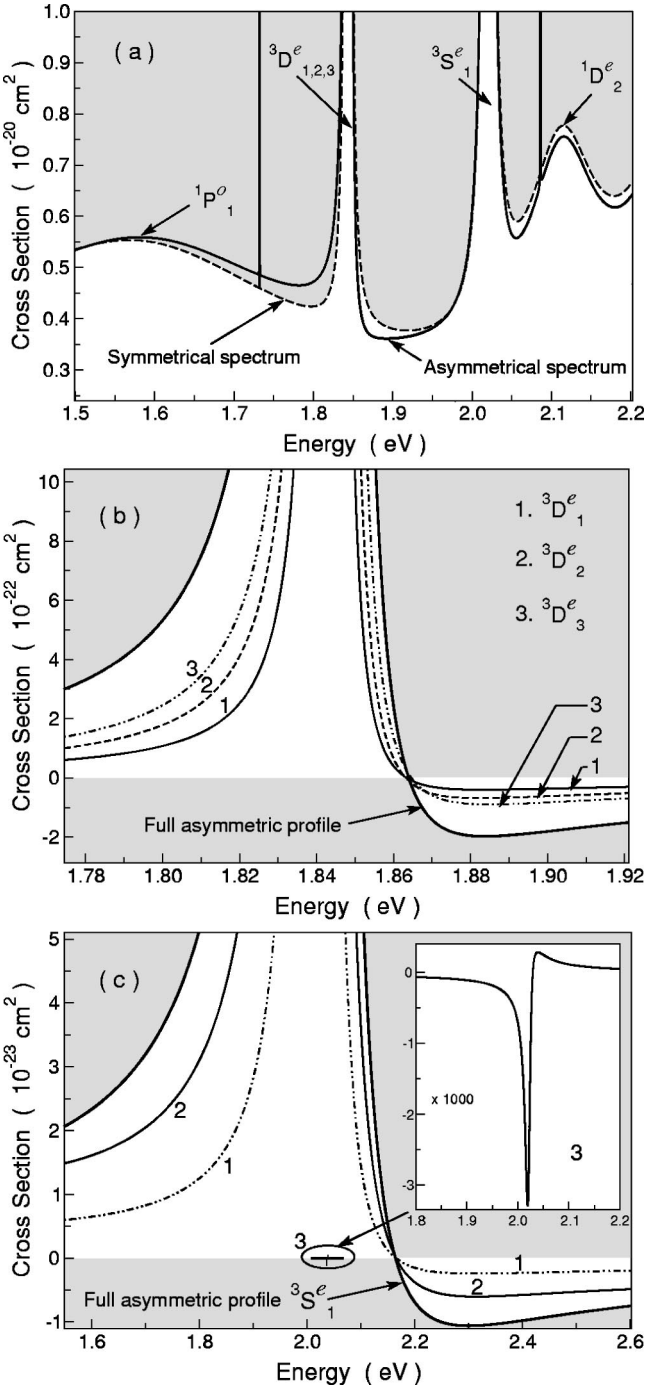

FIG. 6. The calculated recombination cross section with interference effects. (a) The solid line shows the full asymmetric spectrum obtained with Eq. (4) while the dashed line shows the symmetrical part from the same expression. (b) Shows an enlargement of the resonant part of DR cross section formed by the three asymmetric and mutually overlapping resonances $(2p3p)\,{}^3D^e_{1,2,3}$. (c) Enlarged resonant part of the DR cross section coming from asymmetric resonance $(2p3p)\,{}^3S^e_1$ showing its two dominant stabilization channels separately [1. $(2s3p)\,{}^3P^o_1$ and 2. $(2s3p)\,{}^3P^o_2$]; insert: channel 3. $(2s2p)\,{}^3P^o_2$ leads to a quite weak and masked resonance with impressive Beutler-Fano shape. In panels (b) and (c) the nonresonant background is left out in order to make interference more obvious, i.e., the negative values should be interpreted as "below the background."

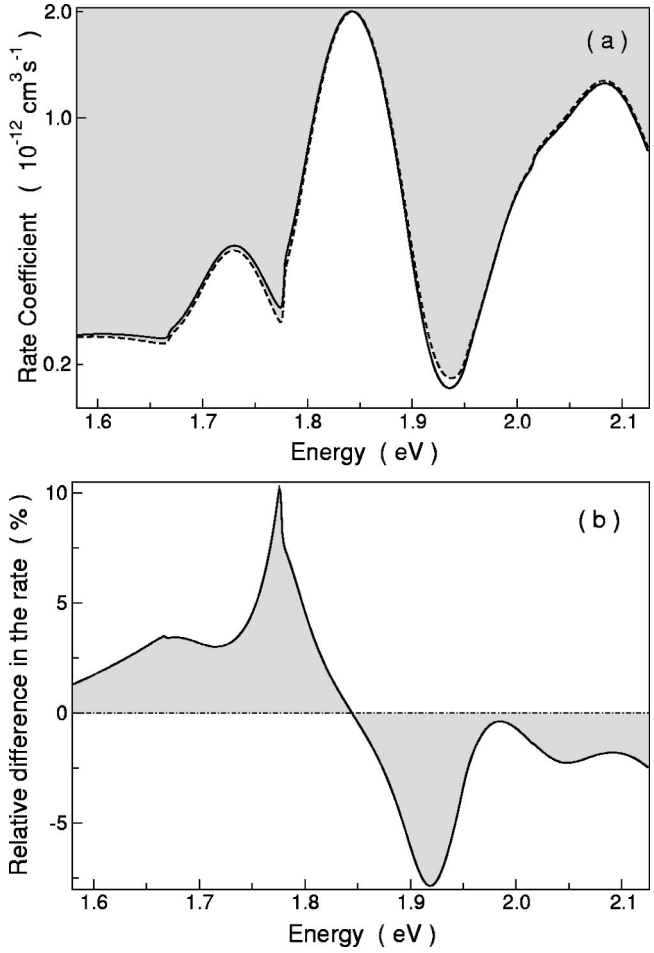

FIG. 7. (a) Recombination rate coefficients in log scale, obtained from folding the calculated asymmetrical (full line) and the symmetrical (dashed line) cross sections in the energy range where interference effects are found. The electron velocity distribution is characterized by $kT_\perp = 1$ meV and $kT_\parallel = 0.22$ meV (for details see text). (b) Relative difference, $(\alpha_{\rm sym}\text{-}\alpha_{\rm asym})/\alpha_{\rm sym}$, in the rate coefficient showing the significance level of the interference effects.

$\leqslant 10^{-3}$ eV, the experimental rate increasingly exceeds the RR calculations by up to a factor of 3.1. This rate enhancement is similar in magnitude to the previously observed enhancement, but is surprisingly large considering that we are dealing with a singly charged ion. The possibility for interference between RR and DR channels has been considered in the calculations. Although this effect could not be observed in the presented experiment, due to the achieved statistical error and resolution, it does not rule out an observation in the future.

ACKNOWLEDGMENTS

The authors would like to thank the CRYRING crew for their efforts in providing the Be beam, and the Swedish Science Research Council (VR) for financial support. T. M. is grateful for support from the Egyptian Government. We have benefited from discussions with Dr. K. B. MacAdam regarding field ionization features.

[1] S. Mannervik *et al.*, Phys. Rev. Lett. **81**, 313 (1998).
[2] P. Glans *et al.*, Phys. Rev. A **64**, 043609 (2001).
[3] P. Glans *et al.*, Nucl. Instrum. Methods Phys. Res. B **154**, 97 (1999).
[4] W. Zong *et al.*, J. Phys. B **31**, 3729 (1998).
[5] T. Bartsch *et al.*, Phys. Rev. Lett. **79**, 2233 (1997).
[6] J. Kenntner *et al.*, Nucl. Instrum. Methods Phys. Res. B **98**, 142 (1995).
[7] W. Zong *et al.*, Phys. Rev. A **56**, 386 (1997).
[8] S. Schippers *et al.*, Phys. Rev. A **62**, 022708 (2000).
[9] G. Kilgus *et al.*, Phys. Rev. **46**, 5730 (1992).
[10] S. Madzunkov *et al.*, Phys. Scr. **92**, 357 (2001).
[11] W. Spies *et al.*, Phys. Rev. Lett. **69**, 2768 (1992).
[12] W. Spies *et al.*, Hyperfine Interact. **108**, 155 (1997).
[13] U. Fano, Phys. Rev. **124**, 1866 (1961).
[14] D.A. Knapp *et al.*, Phys. Rev. Lett. **74**, 54 (1995).
[15] K. Abrahamsson *et al.*, Nucl. Instrum. Methods Phys. Res. B **79**, 269 (1993).
[16] D.R. DeWitt *et al.*, Phys. Rev. A **53**, 2327 (1996).
[17] S. Salomonson and P. Öster, Phys. Rev. A **41**, 4670 (1990).
[18] E. Lindroth, Phys. Rev. A **49**, 4473 (1994).
[19] D.R. DeWitt *et al.*, J. Phys. B **28**, L147 (1995).
[20] E. Lindroth, Hyperfine Interact. **114**, 219 (1998).
[21] M. Tokman *et al.*, Phys. Rev. A **66**, 012703 (2002).
[22] E. Lindroth *et al.*, Phys. Rev. Lett. **86**, 5027 (2001).
[23] T.N. Rescigno and V. McKoy, Phys. Rev. A **12**, 522 (1975).
[24] E. Lindroth, Phys. Rev. A **52**, 2737 (1995).
[25] H. Poth, Phys. Rep. **196**, 136 (1990).
[26] A. Müller, Int. J. Mass Spectrom. Ion Processes **192**, 9 (1999).
[27] R. Martin, *Theory and Design of Charged Particle Beams* (Wiley, New York, 1994).
[28] S.A. Blundell, W.R. Johnson, Z.W. Liu, and J. Sapirstein, Phys. Rev. A **40**, 2233 (1989).
[29] S. Salomonson and A. Ynnerman, Phys. Rev. A **43**, 88 (1991).
[30] L. Johansson, Ark. Fys. **20**, 489 (1961).
[31] A. Kramida and W.C. Martin, J. Phys. Chem. Ref. Data **26**, 1185 (1997).
[32] J.M. Esteva, G. Mehlman-Balloffet, and J. Romand, J. Quant. Spectrosc. Radiat. Transf. **12**, 1291 (1972).
[33] E. Lindroth and A.-M. Mårtensson-Pendrill, Phys. Rev. A **53**, 3151 (1996).
[34] NIST Atomic Spectra Database, WWW published at http://physics.nist.gov.
[35] A. Müller *et al.*, Phys. Rev. A **36**, 599 (1987).
[36] N. Ryde, *Atoms and Molecules in Electric Fields* (Almqvist-Wiksell International, Stockholm, 1976), p. 111.
[37] K.T. Lu, J. Opt. Soc. Am. **64**, 706 (1974).
[38] C.W. Clark *et al.*, J. Opt. Soc. Am. B **2**, 891 (1985).
[39] T.N. Chang, Phys. Rev. A **39**, 4946 (1989).
[40] M.K. Chen, J. Phys. B **31**, 4523 (1998).
[41] R.J. Damburg and V.V. Kolosov, J. Phys. B **11**, 1921 (1978).
[42] R.J. Damburg and V.V. Kolosov, J. Phys. B **12**, 2637 (1979).
[43] D.R. DeWitt *et al.*, Phys. Rev. A **50**, 1257 (1994).
[44] T.N. Chang, Phys. Rev. A **41**, 4922 (1990).
[45] H. Gao *et al.*, J. Phys. B **30**, L499 (1997).
[46] S. Schippers *et al.*, Astrophys. J. **555**, 1027 (2001).
[47] S. Schippers *et al.*, J. Phys. B **31**, 4873 (1998).
[48] G. Gwinner *et al.*, Phys. Rev. Lett. **84**, 4822 (2000).
[49] N. Eklöw *et al.*, Hyperfine Interact. **127**, 251 (2000).
[50] G. Mehlman-Balloffet and J.M. Esteva, Astrophys. J. **157**, 945 (1969).
[51] R. Moccia and P. Spizzo, J. Phys. B **18**, 3537 (1985).